Profile Stiffness Measurements in HSX and comparison to Nonlinear Gyrokinetic Calculations

G M Weir, B J Faber, K M Likin, J N Talmadge, D T Anderson, F S B Anderson

HSX Plasma Laboratory, University of Wisconsin - Madison, Madison, WI, USA

Stiffness measurements are presented in the quasihelically symmetric experiment HSX, in which the neoclassical transport is comparable to that in a tokamak and turbulent transport dominates throughout the plasma. Electron cyclotron emission is used to measure the local electron temperature response to modulated electron cyclotron resonant heating. The amplitude and phase of the heat wave through the steep electron temperature gradient region of the plasma are used to determine a transient electron thermal diffusivity that is close to the steady-state diffusivity. The low stiffness in the region between $0.2 \leq r/a \leq 0.4$ agrees with the scaling of the steady-state heat flux with temperature gradient in this region. These experimental results are compared to gyrokinetic calculations in a flux-tube geometry using the GENE code with two kinetic species. Linear simulations show that the Electron Temperature Gradient (ETG) mode may be experimentally relevant within $r/a \leq 0.2$, while the Trapped Electron Mode (TEM) is the dominant long-wavelength microturbulence instability across most of the plasma. The TEM is primarily driven by the density gradient. Non-linear calculations of the saturated heat flux driven by the TEM and ETG bracket the experimental heat flux.

I. INTRODUCTION

Tokamaks have typically observed temperature profiles that are resilient to changes in the heating deposition profile, i.e. large changes in the electron heat flux lead to only small changes in the electron temperature gradient [1]. This effect has not been observed in conventional stellarators. In W7-AS, it has been shown that the electron temperature profile can vary over a broad range with different heating methods, deposition profiles and confinement regimes [2]. The ratio of the electron thermal diffusivity from transient heat transport experiments to the steady-state diffusivity from power balance is a measure of the stiffness in the electron heat flux. In tokamaks with profile resiliency, the thermal diffusivity obtained from heat pulse propagation is typically much larger than the thermal diffusivity from steady state power balance. In contrast, experiments in LHD [3], W7-AS [4] and TJ-II [5] have shown that heat pulse and power balance diffusivities are comparable.

Electron heat transport experiments in tokamaks have been compared to gyrokinetic calculations [6]. This paper reports the first comparisons between non-linear gyrokinetic calculations and experimental measurements in a stellarator. The saturated electron heat flux driven by the Trapped Electron Mode (TEM) and the Electron Temperature Gradient (ETG) mode are compared to the experimental electron heat flux.

These experiments were done in the Helically Symmetric experiment [7] (HSX), which has a direction of approximately constant magnetic field strength along a helical direction. Previous experimental results have shown that the neoclassical transport is reduced so that the electron heat diffusivity is dominated by anomalous transport [8]. The low neoclassical transport in HSX allows for a study of profile resiliency and stiffness in the electron heat flux in an optimized stellarator.

Experimental measurements of the electron heat flux are introduced in Section II, and linear and non-linear gyrokinetic calculations are compared to these measurements in Section III.

II. ELECTRON HEAT TRANSPORT MEASUREMENTS

The power balance thermal diffusivity is the ratio of the normalized heat flux with respect to temperature gradient, $\chi_e^{PB} = -q_e/(n_e \nabla T_e)$, while the heat pulse diffusivity is

a measure of the local gradient of the heat flux with respect to temperature gradient, $\chi_e^{HP} = -\partial q_e/(n_e \partial \nabla T_e)$ [9]. The stiffness in the electron heat flux is parameterized by the logarithmic gradient of the heat flux with respect to the temperature gradient. The stiffness is experimentally quantified by the ratio of thermal diffusivities measured using transient and steady-state techniques, $\partial \ln q_e/\partial \ln \nabla T_e = \chi_e^{HP}/\chi_e^{PB}$ [10]. Steady-state and transient transport analysis techniques are used concurrently to determine the experimental stiffness in the electron heat flux and to investigate anomalous heat transport in HSX.

To measure the stiffness, two sets of Electron Cyclotron Resonance Heating (ECRH) experiments have been conducted. In the first experiment, the ECRH resonance location was moved across the plasma to change the temperature gradient in the region of $0.2 \leq r/a \leq 0.4$. In the second experiment, the launched ECRH power was modulated with on-axis heating to facilitate measurements of the transient electron thermal diffusivity in the same region. The density profiles were matched between both experiments.

Figure 1 shows the electron temperature and plasma density measured by a 10 spatial channel Thomson scattering diagnostic during the ECRH resonance scan. The resonance location was moved from $r/a = 0.3$ on the inboard side of the plasma to $r/a = 0.2$ on the outboard side of the plasma by changing the on-axis magnetic field from $|B_o| = 0.96$T to $|B_o| = 1.02$T. The core electron temperature measured by Thomson scattering varied between 400 and 1200 eV. Three of the electron temperature profiles are shown in color for easy comparison with the absorbed power profiles shown in Figure 2.

Two ECRH antennas are used on HSX. Previous measurements with on-axis heating show that the absorption of the ordinary wave is localized within $r/a \leq 0.2$ [11]. The profile shape and total absorption are reproduced by a multi-pass ray tracing model using the TRAVIS code [12]. The absorbed power profile for each case in Figure 1 is shown in Figure 2. As the cyclotron resonance is moved away from the magnetic axis, the electron temperature becomes less peaked and flattens inside the radius of the peak absorption. The temperature gradient within $0.2 \leq r/a \leq 0.4$ decreases with off-axis heating, while the volume average electron temperature across this region varies by less than 100 eV.

There are no significant electron energy sinks in the region of the plasma considered during these experiments. The total radiated power is less than 5 kW and localized to the outer half-radius, and the collisional coupling to ions is small, because the plasma density in HSX is limited by the cut-off density of the ordinary wave, 1×10^{19}m^{-3}. Consequently,
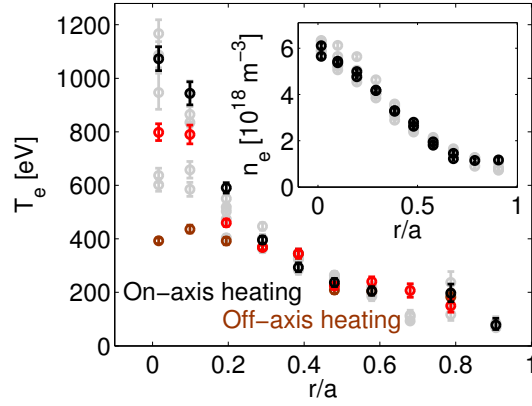
FIG. 1. Eight Thomson scattering profiles of the electron temperature and plasma density measured during an ECRH resonance scan (gray). Heating on-axis ($r/a \approx 0$, black), off-axis ($r/a \approx 0.3$, brown), and an intermediate point ($r/a \approx 0.1$, red).
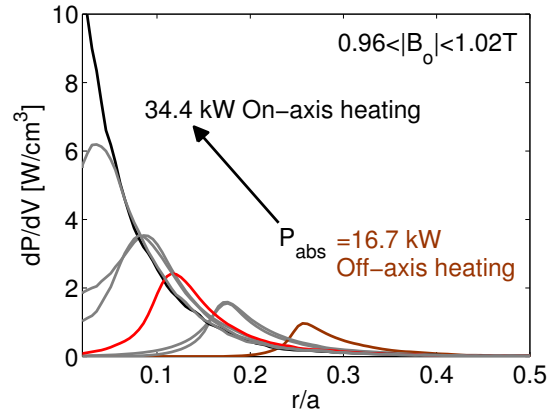

FIG. 2. Multi-pass ray tracing calculations of the absorbed power profile from an ECRH resonance scan (gray) shown in Figure 1. Heating on-axis ($r/a \approx 0$, black), off-axis ($r/a \approx 0.3$, brown), and an intermediate point ($r/a \approx 0.1$, red).

the experimental heat flux is estimated by the total power deposited by the ECRH within a flux surface, divided by the flux surface area.

During the ECRH modulation experiment, the power launched from the first antenna was scanned from 25 to 50 kW, while the power launched from the second antenna was held at 50 kW and modulated by 10%. The power deposition profile shape did not change during this second experiment, but the total absorbed power increased with the launched ECRH power. The volume average heat flux over the region that heat pulse propagation data is

available, $0.2 \leq r/a \leq 0.4$ (the foot of the steep electron temperature gradient region), is plotted as a function of electron temperature gradient scale length, $a/L_{Te} = -a\nabla T_e/T_e$, for both experiments in Figure 3. The heat flux scales linearly with temperature gradient between $1.8 \leq a/L_{Te} \leq 3$, and the average density gradient scale length was held constant at $a/L_{ne} = 2.5 \pm 0.1$ in both experiments.
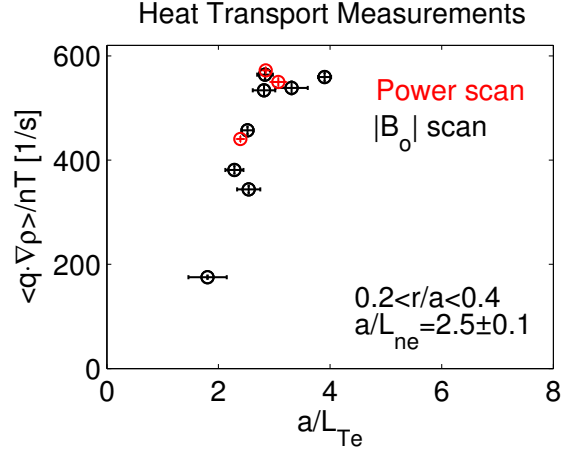

FIG. 3. Normalized heat flux, volume-averaged between $0.2 \leq r/a \leq 0.4$, versus temperature gradient scale length in ECRH power and resonance location scans.

The power balance diffusivity is determined using a standard transport analysis,

$$\chi_e^{PB}(\rho) = -\frac{\langle \vec{q}_e \cdot \nabla\rho \rangle}{n_e \langle |\nabla\rho|^2 \rangle \frac{\partial T_e}{\partial\rho}} = -\frac{\int_0^\rho P_e(\rho')V'(\rho')d\rho'}{V' n_e \langle |\nabla\rho|^2 \rangle \frac{\partial T_e}{\partial\rho}}. \tag{1}$$

Here $V' = \frac{\partial V}{\partial\rho}$, V is the volume enclosed by a flux surface and $\rho = r/a$ is the square root of the toroidal flux normalized to the value at the edge. The factors V' and $\nabla\rho$ arise from the deviations of the plasma shape from a cylinder. P_e is the power density deposited by the ECRH and the numerator on the right hand side is the total power deposited up to the flux surface defined by ρ. The plasma density, n_e, and the electron temperature, T_e, are both measured by Thomson scattering. The density and temperature profiles for on-axis heating during the ECRH modulation experiments are shown in Figure 4. The core electron temperature increases from 600 eV to 1200 eV as the absorbed power is increased from 19 kW to 34 kW.

The χ_e^{PB} profiles corresponding to the profiles of Figure 4 are shown in Figure 5. The power balance thermal diffusivities between $0.2 \leq r/a \leq 0.4$ are similar and the volume average diffusivity across this region is tabulated versus absorbed power in Table I. Within
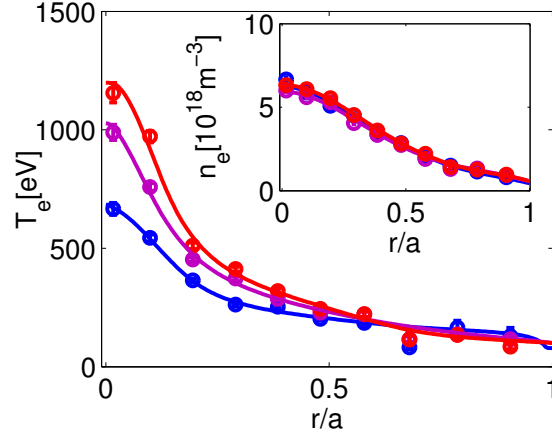
FIG. 4. The electron temperature and density profiles measured by Thomson scattering for on-axis heating at three absorbed powers, 19 kW (blue), 29 kW (magenta), and 34 kW (red).

$r/a \leq 0.4$, the thermal diffusivity profile is almost the same, which is indicative of electron heat transport that is not stiff.
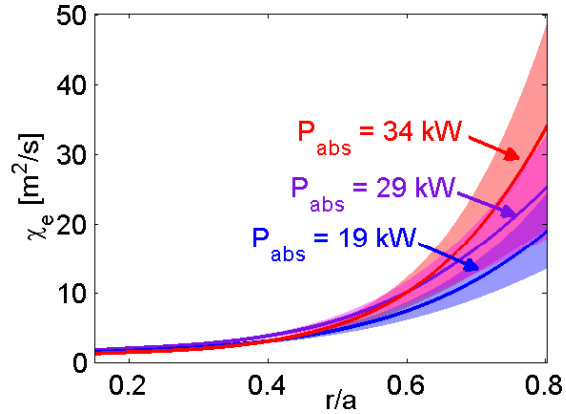

FIG. 5. The electron thermal diffusivity from a power balance analysis for on-axis heating is shown at three absorbed powers, 19 kW (blue), 29 kW (magenta), and 34 kW (red).

Heat pulse propagation measurements of the transient electron thermal diffusivity require a spatially localized and time-resolved electron temperature diagnostic. The temporal evolution of the electron temperature is measured using an absolutely calibrated Electron Cyclotron Emission (ECE) diagnostic. The 16 channel heterodyne radiometer gathers emission between 50-62 GHz, corresponding to resonance locations within $r/a < 0.5$ on both sides of the magnetic-axis, and each channel has 300 kHz of video bandwidth. Although

the Low-Field Side (LFS) and the High-Field Side (HFS) channels are symmetric across the plasma, and in good agreement with Thomson scattering measurements of the electron temperature at moderate heating powers, the LFS channels may sample relativistically down-shifted emission from the core in the hot plasma analyzed in this work. Consequently, only the HFS channels are used in heat pulse propagation experiments.

The temporal response of the electron temperature to modulated heating carries heat transport information at the modulation frequency in the amplitude, T_ω, and phase, φ_ω, between radially separated channels of the ECE radiometer.

A representative time-trace of the HFS ECE channels from a plasma discharge is shown in Figure 6. There is a strong response in the electron temperature to square wave ECRH modulation at 460 Hz. This is evident in the power spectral density that is also shown in Figure 6, which results from averaging the power spectrum of the electron temperature from four 13 ms time-windows.
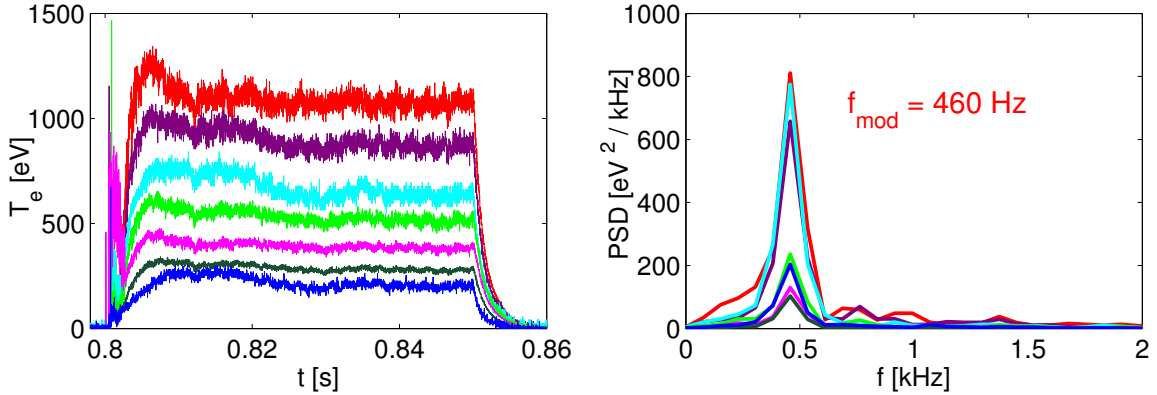

FIG. 6. The ECE electron temperature versus time (at left) and the Power Spectral Density (PSD) of that electron temperature (at right) from a representative plasma discharge with ECRH modulation.

The heat pulse thermal diffusivity is determined from the logarithmic amplitude and the phase in cylindrical geometry by

$$\chi_{e,eff}^{HP} = -\frac{3}{4}\frac{\omega_{mod}}{\left\langle |\nabla\rho|^2 \right\rangle}\left[\frac{d\varphi_\omega}{d\rho}\left(\frac{d\ln T_\omega}{d\rho} + \frac{1}{2\rho} + \frac{1}{2}\frac{d\ln n_e}{d\rho}\right)\right]^{-1}. \qquad (2)$$

Equation 2 is the cylindrical model from [13] with the radial coordinate replaced by the effective radius, and the heat pulse diffusivity replaced by the effective heat pulse diffusivity, $\left\langle |\nabla\rho|^2 \chi_e^{HP} \right\rangle \approx \chi_e^{HP}\left\langle |\nabla\rho|^2 \right\rangle$. The logarithmic amplitude and phase of the electron

temperature perturbation are determined from Fourier analysis of the pulse propagation at the modulation frequency, ω_{mod}, and the background density gradient scale length from Thomson scattering measurements of the electron density profile.

The phase of the radially separated ECE channels is measured with respect to the ECRH modulation reference signal. The ECE channels used to determine the amplitude and phase of the heat wave have coherence greater than 80% with the reference. The ECE data is shown in Figure 7. The inner limit for the analysis region is set by the radial extent of the modulated source calculated from ray tracing, $r/a \geq 0.2$, and a requirement on the optical depth sets the outer limit for the analysis region, $\tau \geq 0.3$ such that $r/a \leq 0.4$. Multiple shots with similar plasma parameters and slightly different magnetic field values are combined to increase the spatial resolution of heat pulse propagation experiments. However, the perturbation amplitude and phase are offset by a small amount between shots. The heat pulse diffusivity is dependent on the radial derivative of these quantities, which is independent of the offset. The amplitude and phase used in the analysis and shown in Figure 7 have the offset removed.

The derivative of the fits in Figure 7 are used in Equation 2 to determine the heat pulse diffusivities shown in Table I. The stiffness is just below unity for all three powers. This model assumes that the heat flux is diffusive. However, because of finite particle sourcing in the plasma core, it is possible that convective heat transport might also be important. No significant change in diffusivity was measured with modulation frequencies varying between 200 Hz and 1000 Hz, indicating that the core convective heat flux is small. An upper bound on this effect was estimated using the DEGAS code [14] and a suite of absolutely calibrated H_α detectors as discussed in reference [8]. Including the convective heat flux in the transport analysis results in, at most, a 15% decrease in χ_e^{PB} in the region $0.2 \leq r/a \leq 0.4$, and an increase in χ_e^{HP} by a similar amount [13]. The net effect is to make the stiffness closer to one.

TABLE I. Power-balance and heat-pulse diffusivities, and the resulting stiffness, are tabulated versus absorbed power.

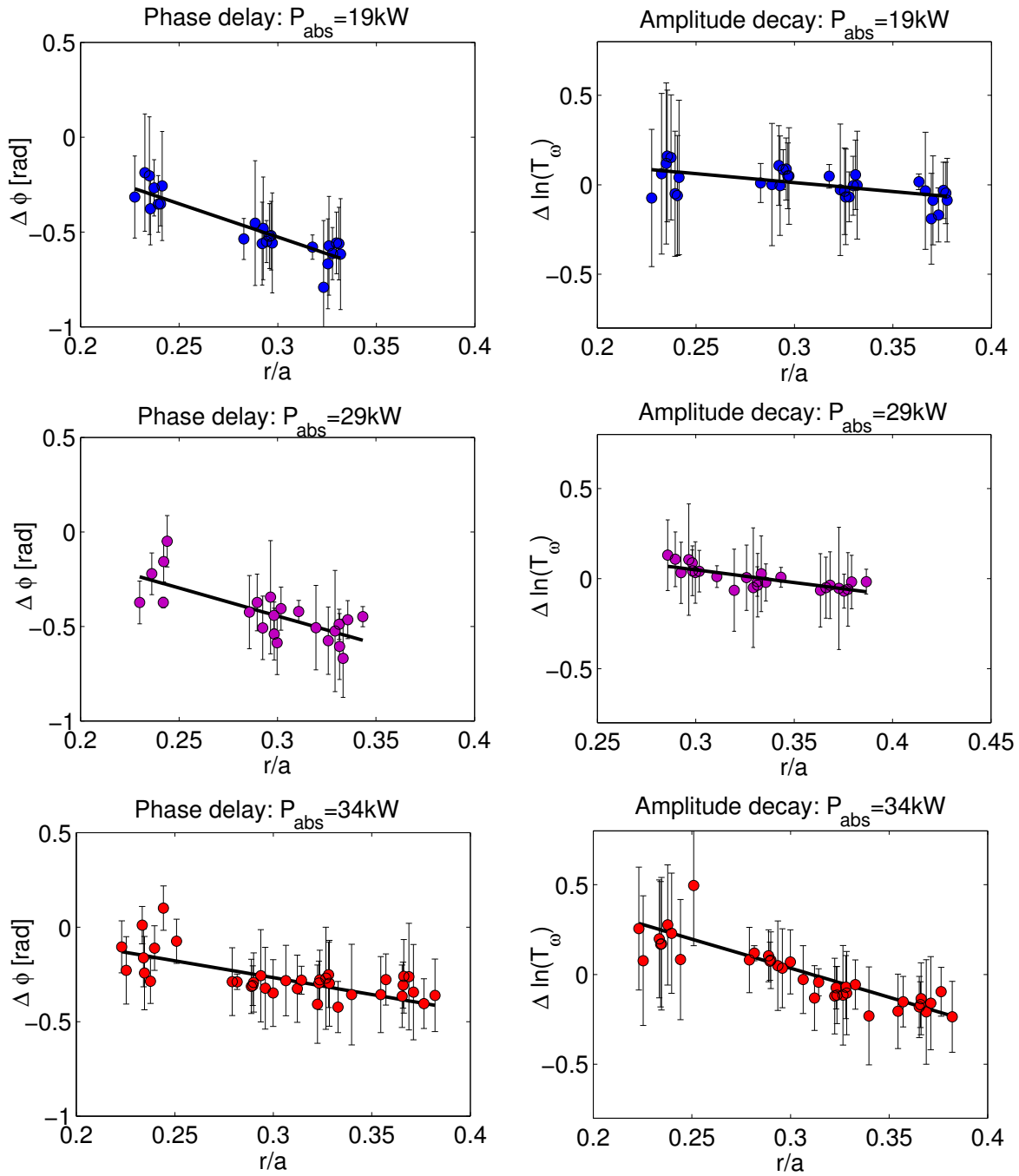| P_{abs}	χ_e^{PB} [m^2/s]	χ_e^{HP} [m^2/s]	χ_e^{HP}/χ_e^{PB}
19 kW	2.4 ± 0.2	1.7 ± 0.2	0.7 ± 0.1
29 kW	2.9 ± 0.2	1.9 ± 0.4	0.7 ± 0.1
34 kW	2.3 ± 0.2	2.1 ± 0.4	0.9 ± 0.2

FIG. 7. The phase delay (left column) and logarithmic amplitude (right column) at the ECRH modulation frequency for three heat pulse propagation experiments with different absorbed powers: 19 kW (1st row), 29 kW (2nd row), and 34 kW (3rd row).

III. COMPARISON TO GYROKINETIC CALCULATIONS

HSX is optimized for neoclassical transport, but is not optimized for anomalous transport driven by turbulent microinstabilities. The non-planar magnetic axis and high effective transform of HSX lead to large normal curvature and short connection lengths [15]. The regions of bad normal curvature and particle trapping are highly correlated, and previous linear gyrokinetic modeling has indicated that the Trapped Electron Mode (TEM) is highly localized in the bad curvature region of HSX [16]. Combined with temperature or density gradients, there is strong drive for curvature driven modes such as the TEM [17].

Figure 8 shows the normal curvature and magnetic field strength in normalized units as a function of helical angle for the most and least unstable flux tubes in HSX. The most unstable flux tube samples the region of low magnetic field strength at the outboard mid-plane of HSX. The least unstable flux tube samples the region of low magnetic field strength on the inboard side of the device. In both flux tubes, the regions of bad normal curvature and particle trapping overlap significantly.
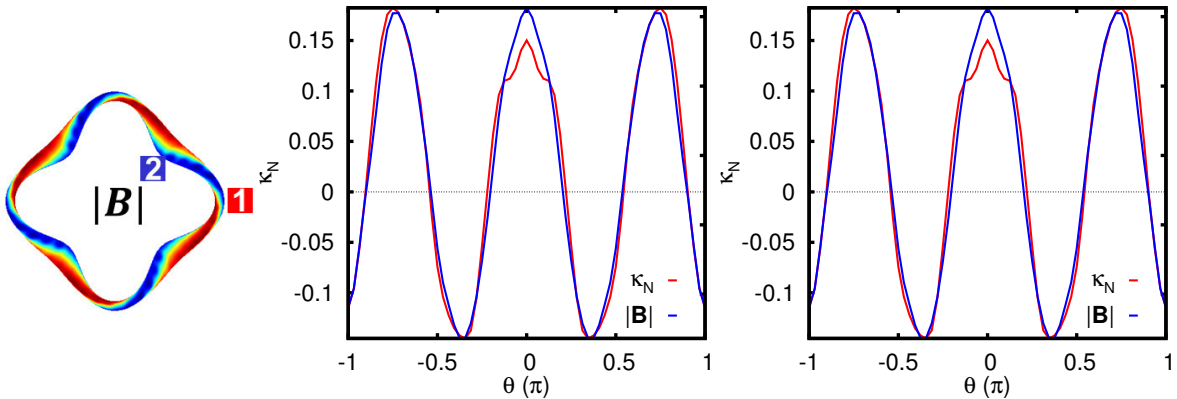

FIG. 8. The normal curvature and magnetic field strength (normalized units) are shown for the most (1, left) and least (2, right) unstable flux-tubes in HSX as a function of helical angle. A plan view of the magnetic field strength (high field in red, low field in blue) at the half-radius is also shown.

The Gyrokinetic Electromagnetic Numerical Experiment (GENE) [18] is used to model micro-instabilities in HSX. GENE solves the Vlasov-Maxwell system of equations for the change in the perturbed distribution function due to gyro-radius scale instabilities. Simulations of micro-instabilities on HSX are collisionless, electrostatic ($\beta \ll 1$) calculations in
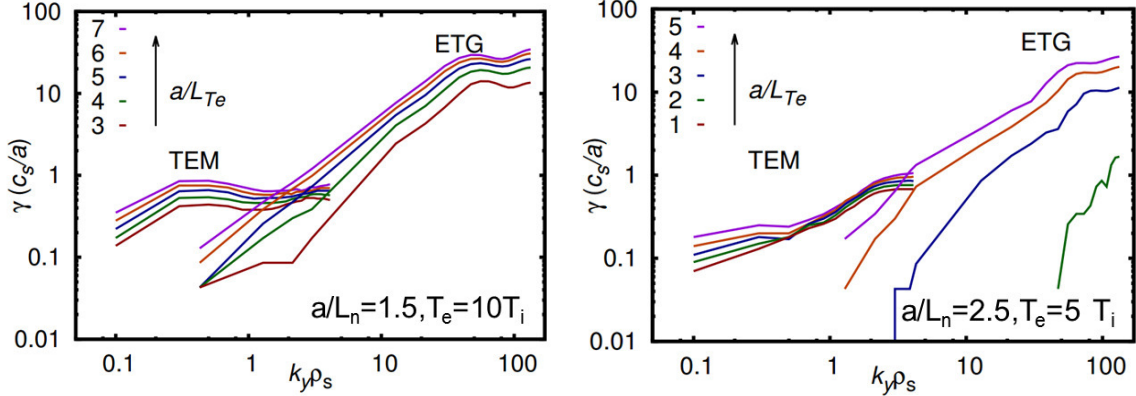
FIG. 9. The linear growth rates of the TEM and the ETG mode versus normalized wave number in the most unstable flux tube at low (left) and high (right) density gradient scale length.

the three-dimensional flux-tube geometry calculated by the GIST code [19]. The TEM is simulated using kinetic electrons and ions, while the Electron Temperature Gradient (ETG) mode is simulated using kinetic electrons and adiabatic ions.

Linear gyrokinetic calculations at TEM and ETG scales indicate that the TEM is linearly unstable for all accessible parameters in HSX. For a density gradient scale length of $a/L_{ne} = 1.5$ and the experimental temperature gradients, the ETG mode is unstable as shown in Figure 9. At the higher density gradient scale length, $a/L_{ne} = 2.5$, Figure 9 shows that the TEM is only weakly dependent on the temperature gradient, and is primarily driven by the density gradient. In this case, the ETG mode is stabilized by the increased density gradient and a linear critical gradient exists between $0.4 \leq \eta_{e,c} \leq 0.8$, where $\eta_e = L_{ne}/L_{Te}$. HSX has very low magnetic shear, and this calculation is consistent with previous estimates of the critical gradient for ETG modes in a shearless slab, $\eta_{e,c} = 2/3$ [20].

At left in Figure 10 are the experimental temperature and density gradient scale lengths for the three heat pulse propagation experiments described in Section II. The temperature is peaked in the core, and the temperature gradient scale length increases with heating power. From quasi-linear estimates, the ETG mode is expected to drive significant transport in nonlinear simulations when the ratio of the ETG to TEM growth rate in linear simulations is comparable to the separation in scales between the modes. This is true in the low-density gradient case ($a/L_{ne} = 1.5$), but this is not true in the high-density gradient case ($a/L_{ne} = 2.5$). The growth rates of the TEM and ETG modes at the maximum in the quasi-linear heat flux for the two density gradients are shown in Figure 10 versus normalized

temperature gradient. In the low-density gradient case, the growth rate of the ETG mode is the square-root of the ion to electron mass ratio larger than the TEM growth rate. This case is representative of the inner 20% of the HSX minor radius, where ETG may be important, and the simulated density gradient is comparable to experiment. However, this is not true at the foot of the steep electron temperature gradient region where the average density gradient scale length is $a/L_{ne} = 2.5$, and the TEM is the dominant microinstability. The high density gradient scale length case is representative of the experimental parameters in the region that heat pulse propagation data is available.

The saturated heat flux driven by the TEM is significantly higher than the saturated heat flux driven by the ETG mode in non-linear simulations of the most unstable flux tube of HSX. At left in Figure 11, the electron heat flux normalized by the gyro-Bohm heat flux in hybrid units, $Q_e^{GB} = n_e T_e c_s (\rho_s/a)^2$, is shown for two flux tubes, the most and least unstable flux tubes in HSX. At right in Figure 11, the saturated electron heat flux driven by the ETG mode is shown in electron units, $Q_e^{GB} = n_e T_e c_e (\rho_e/a)^2$. To put the heat flux driven by the ETG mode into the hybrid units, the ETG result should be divided by the square root of the mass ratio. This results in significantly smaller heat flux from the ETG mode than is calculated for the TEM.

The saturated heat fluxes are compared to the experimental heat flux normalized by the gyro-Bohm heat flux (hybrid units) in Figure 12. The experimental heat flux (from both the resonance and power scan) is shown in black. Although the volume average electron temperature changed by less than 100 eV in the region considered, the strong temperature
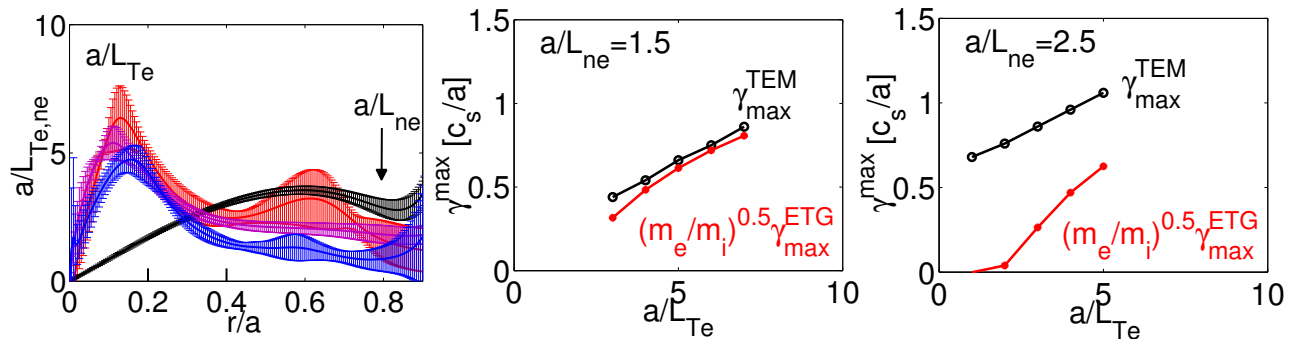

FIG. 10. The experimental density (black) and temperature gradients at three launched powers: 19 kW (blue), 29 kW (magenta), 34 kW (red). The growth rate of the TEM and ETG modes at the maximum quasi-linear heat flux for $a/L_{ne} = 1.5$ (middle), and $a/L_{ne} = 2.5$ (right).
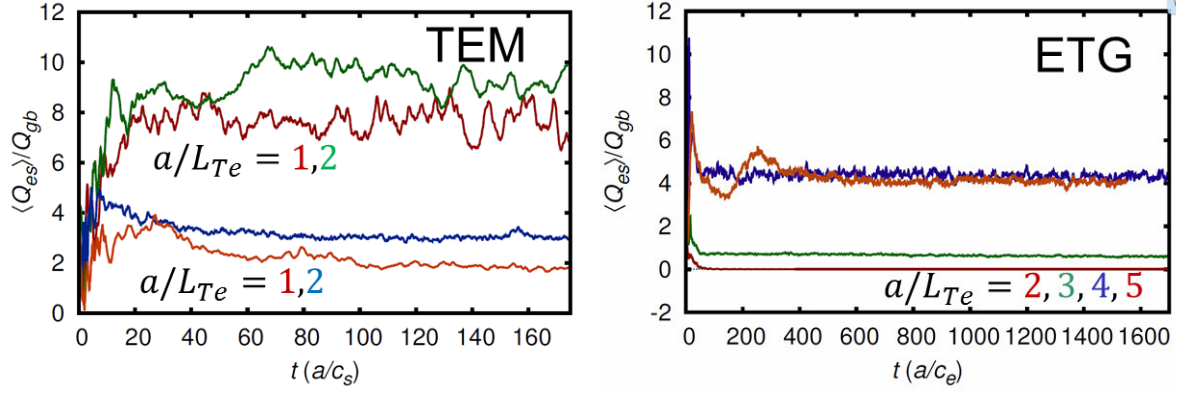
FIG. 11. Non-linear simulations of the electron heat flux driven by the TEM in two flux tubes at two temperature gradients (left), and non-linear simulations of the electron heat flux driven by the ETG mode in the most unstable flux tube (right).

scaling of the gyro-Bohm heat flux ($Q_e^{GB} \propto T_e^{5/2}$), alters the scaling of the experimental heat flux between Figure 3 and Figure 12. The non-linear calculation shows that the ETG mode drives a comparatively low level of transport, but it does reproduce the critical gradient that was predicted by the linear model. The saturated heat flux driven by the TEM is larger than the experimental values.
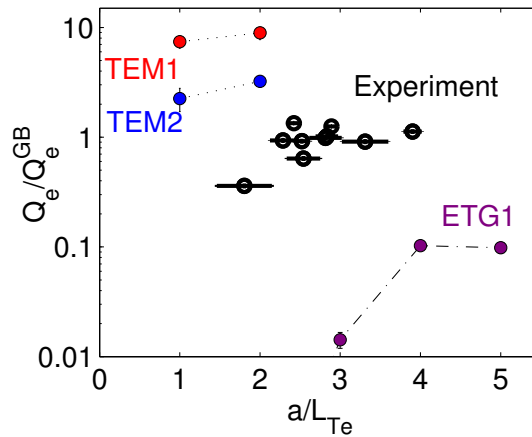

FIG. 12. The heat flux driven by the ETG mode (scaled to hybrid units in purple) in the most unstable flux tube, and the heat flux driven by the TEM in the most (red) and least (blue) unstable flux tube are compared to the experimental heat flux in HSX (black) for fixed $a/L_{ne} = 2.5$.

IV. CONCLUSIONS

In this paper, the first comparisons of non-linear gyrokinetic calculations and experimental heat flux measurements are presented in the quasihelically symmetric experiment HSX. The amplitude and phase of the perturbation through the steep electron temperature gradient region of the plasma are used to determine a transient electron thermal diffusivity and it is approximately equal to the steady-state diffusivity. The low stiffness between $0.2 \leq r/a \leq 0.4$ agrees with the scaling of the steady-state heat flux with temperature gradient in this region. These experimental results have been compared to gyrokinetic calculations using the GENE code with two kinetic species. Linear simulations show that the Electron Temperature Gradient (ETG) mode may be experimentally relevant within $r/a \leq 0.2$, while the Trapped Electron Mode (TEM) is the dominant long-wavelength microturbulence instability across most of the plasma. The TEM is primarily driven by the plasma density gradient. Non-linear calculations of the saturated heat flux driven by the TEM and ETG bracket the experimental heat flux.

ACKNOWLEDGEMENTS

REFERENCES

[1] J.C. DeBoo, C.C. Petty, A.E. White, K.H. Burrell, E.J. Doyle, J.C. Hillesheim, C. Holland, G.R. McKee, T.L. Rhodes, L. Schmitz *et al.*, Physics of Plasmas **19**, 082518 (2012).

[2] F. Wagner, M. Hirsch, H-J Hartfuss, H.P. Laqua and H. Maassberg, Plasma Phys. Control. Fusion **48**, A217 (2006).

[3] S. Inagaki, H. Takenaga, K. Ida, A. Isayama, N. Tamura, T. Takizuka, T. Shimozuma, Y. Kamada, S. Kubo, Y. Miura *et al.*, Nucl. Fusion **46**, 133 (2006).

[4] M. Hirsch, J. Baldzuhn, C. Beidler, R. Brakel, R. Burhenn, A. Dinklage, H. Ehmler, M. Endler, V. Erckmann, Y. Feng *et al.*, Plasma Phys. Control. Fusion **50**, 053001 (2008).

[5] S. Eguilior, F. Castejon, E. de la Luna, A. Cappa, K. Likin, A Fernandez and TJ-II Team, Plasma Phys. Control. Fusion **45**, 105 (2003).

[6] F. Ryter, Y. Camenen, J.C. DeBoo, F. Imbeaux, P. Mantica, G. Regnoli, C. Sozzi, U. Stroth and Asdex Upgrade and DIII-D Teams *et al.*, Plasma Phys. Control. Fusion **48**, B453 (2006).

[7] F.S.B. Anderson, A.F. Almagri, D.T. Anderson, P.G. Matthews, J.N. Talmadge, J.L. Shohet, Fusion Technol. **27**, 273 (1995).

[8] J.M. Canik, D.T. Anderson, F.S.B. Anderson, C. Clark, K.M. Likin, J.N. Talmadge and K. Zhai, Phys. Plasmas **14**, 056107 (2007).

[9] F. Ryter, C. Angioni, M. Beurskens, S. Cirant, G.T. Hoang, G.M.D. Hogeweij, F. Imbeaux, A. Jacchia, P. Mantica, W. Suttrop, G. Tardini, Plasma Phys. Control. Fusion **43**, A323 (2001).

[10] U. Stroth, Plasma Phys. Control. Fusion **40** (1998)

[11] G.M. Weir, Ph.D. dissertation University of Wisconsin, 2014.

[12] N.B. Marushchenko, V. Erckmann, H.J. Hartfuss, M. Hirsch, H.P. Laqua, H. Maassberg, Y. Turkin, Plasma and Fusion Research. **2**, S1129 (2007).

[13] A. Jacchia, P. Mantica, F. De Luca, and G. Gorini, Physics of Fluids B **3**, 3033 (1991).

[14] D. Heifetz, D. Post, M. Petravic, J. Weisheit, and G. Bateman, J. Comput. Phys. **46**, 309 (1982).

[15] G. Rewoldt, L. P. Ku, and W. M. Tang, Phys. Plasmas **12**, 102512 (2005).

[16] W. Guttenfelder, J. Lore, D.T. Anderson, F.S.B. Anderson, J.M. Canik, W.M. Dorland, K.M. Likin, J.N. Talmadge, Phys Rev Lett. **101**, 215002 (2008).

[17] B.B. Kadomtsev and O.P. Pogutse, Soviet Physics JETP **24**, 1172 (1967).

[18] F. Jenko, W. Dorland, M. Kotschenreuther, and B.N. Rogers, Phys. Plasmas **7**, 5 (2000).

[19] P. Xanthopoulos, W. A. Cooper, F. Jenko, Yu. Turkin, A. Runov, and J. Geiger, Phys. Plasmas **16**, 082303 (2009).

[20] W. Horton, G. T. Hoang, C. Bourdelle, X. Garbet, M. Ottaviani, and L. Colas, Phys. Plasmas **11**, 2600 (2004).